

Controlled DC Monitoring of a Superconducting Qubit

A. Kringhøj,¹ T. W. Larsen,¹ B. van Heck,^{2,3} D. Sabonis,¹ O. Erlandsson,¹
I. Petkovic,¹ D. I. Pikulin,² P. Krogstrup,^{1,4} K. D. Petersson,¹ and C. M. Marcus¹

¹Microsoft Quantum Lab Copenhagen and Center for Quantum Devices, Niels Bohr Institute, University of Copenhagen, Universitetsparken 5, 2100 Copenhagen, Denmark

²Microsoft Quantum, Station Q, University of California, Santa Barbara, California 93106-6105, USA

³Microsoft Quantum Lab Delft, Delft University of Technology, 2600 GA Delft, The Netherlands

⁴Microsoft Quantum Materials Lab Copenhagen, Kanalvej 7, 2800 Lyngby, Denmark

Creating a transmon qubit using semiconductor-superconductor hybrid materials not only provides electrostatic control of the qubit frequency, it also allows parts of the circuit to be electrically connected and disconnected *in situ* by operating a semiconductor region of the device as a field-effect transistor (FET). Here, we exploit this feature to compare *in the same device* characteristics of the qubit, such as frequency and relaxation time, with related transport properties such as critical supercurrent and normal-state resistance. Gradually opening the FET to the monitoring circuit allows the influence of weak-to-strong DC monitoring of a “live” qubit to be measured. A model of this influence yields excellent agreement with experiment, demonstrating a relaxation rate mediated by a gate-controlled environmental coupling.

Josephson junctions (JJs) serve as key elements in a wide range of quantum systems of interest for fundamental explorations and technological applications. JJs, which provide the nonlinearity essential for superconducting qubits [1], are typically fabricated using insulating tunnel junctions between superconducting metals [2]. Alternative realizations using atomic contacts [3] or superconductor-semiconductor-superconductor (S-Sm-S) junctions [4–6] are receiving growing attention. Hybrid S-Sm-S JJs host a rich spectrum of new phenomena, including a modified current-phase relation (CPR) [7, 8] different from the sinusoidal CPR of metal-insulator-metal tunnel junctions. Other electrostatically tunable parameters include the sub-gap density of states (DOS), shunt resistance [9], spin-orbit coupling [10], and critical current [11].

Recent work on S-Sm-S JJs in various platforms relies on either DC (direct current) transport [8, 12] or cQED (circuit quantum electrodynamics) measurements [13–16]. Common to these experiments is that valuable device information is only accessible in one of the two measurement techniques. For instance, measurements estimating individual transmission eigenvalues [17] or measurements probing the local DOS are directly accessible with DC transport but not with cQED. The prospect of combining these techniques potentially allows a deeper understanding of JJ-based quantum systems.

In this Letter, we investigate a modified S-Sm-S JJ design of a gatemon qubit that combines DC transport and coherent cQED qubit measurements. The device is realized in an InAs nanowire with a fully surrounding epitaxial Al shell by removing the Al layer in a second region (besides the JJ itself) allowing that region to function as a field-effect transistor (FET). By switching the FET between being conducting (“on”) or depleted (“off”) using a gate voltage, we are able to implement a controlled transition between the transport and cQED measure-

ment configurations. We demonstrate that the additional tunability does not compromise the quality of the qubit

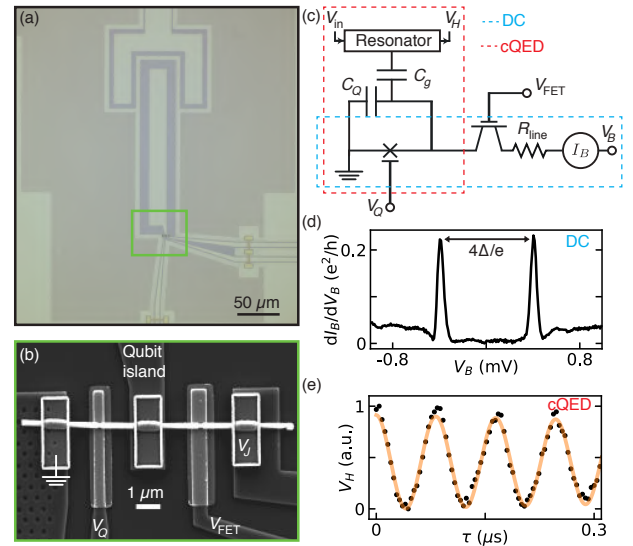


FIG. 1. (a) Optical micrograph of the modified gatemon qubit-device showing the bottom of the readout resonator capacitively coupled to the qubit island. The island is contacted to a nanowire placed in the highlighted green square. (b) Scanning electron micrograph (SEM) of the nanowire in the green rectangle in (a). Two removed segments of the Al shell form the qubit JJ (125 nm) and the FET (175 nm), controlled by gates V_Q and V_{FET} . The bias voltage across the nanowire is indicated V_J . (c) Device circuit with FET off for cQED (dashed red box), and FET on allowing transport (dashed blue box). The bias voltage V_B refers to the total voltage drop across both the nanowire and line resistance R_{line} . (d) Differential conductance dI_B/dV_B as a function of bias voltage V_B shows the superconducting gap Δ of the qubit JJ, with $V_{FET} = +4$ V and $V_Q = -2.9$ V. (e) Rabi oscillations of the qubit seen in resonator output V_H as a function of drive time τ at $V_{FET} = -3$ V and $V_Q = -2.5$ V, with exponentially damped sinusoid (orange).

in the cQED configuration, where the FET is off. We further demonstrate control of the qubit relaxation as the FET is turned on, continuously increasing the coupling of the junction to the environment, in agreement with a simple circuit model. Finally, we demonstrate strong correlation between cQED and transport data by comparing the measured qubit frequency spectrum with the switching current directly measured *in situ*.

Devices were fabricated on a high resistivity silicon substrate covered with a 20 nm NbTiN film. The nanowire region, qubit-capacitor island, electrostatic gates, on-chip gate-filters, readout resonator, and transmission line were patterned by electron-beam lithography and defined by reactive-ion etching techniques, see Fig. 1(a). The full-shell InAs/Al epitaxial hybrid nanowire is placed at the bottom of the qubit island, see Fig. 1(b) [18]. Two gateable regions are formed by selective wet-etching of the Al in two ~ 150 nm segments defined by electron-beam lithography, aligned with two independent bottom gates, which are separated from the nanowire by a 15 nm thick HfO₂ dielectric. The three superconducting segments—ground, qubit island with capacitance C_Q , and DC bias V_J —are then contacted with ~ 200 nm sputtered NbTiN, see Fig. 1(b). In this circuit, when the FET is on, DC current/voltage measurements are available [blue box in Fig. 1(c)]. Depleting the FET allows the device to operate as a qubit, where measurements of the heterodyne demodulated transmission V_H allow qubit state determination and V_Q allows tuning the qubit frequency f_{01} over several GHz [red box in Fig. 1(c)].

Setting the voltage on the FET gate to $V_{\text{FET}} = +4$ V, which turned the FET fully conducting, and the voltage on the qubit JJ to $V_Q = -2.9$ V makes the voltage drop predominantly across the qubit JJ. In this configuration, the differential conductance dI_B/dV_B , probes the convolution of the DOS on each side of the JJ, see Fig. 1(d). Keeping in mind a simple model of JJ spectroscopy [9], we interpret the distance between the two peaks in dI_B/dV_B as $4\Delta/e = 4 \times 190 \mu\text{V}$, where Δ is the induced superconducting gap. In the cQED configuration, with $V_{\text{FET}} = -3$ V and $V_Q = -2.5$ V, coherent Rabi oscillations are observed by varying the duration τ of the qubit drive tone at the qubit frequency $f_{01} = 4.6$ GHz. Following the drive tone, a second tone was applied at the readout resonator frequency, $f_R \sim 5.3$ GHz, to perform dispersive readout where V_H is measured, see Fig. 1(e). These experiments are carried out in a dilution refrigerator with a base temperature of ~ 10 mK using standard lock-in and DC techniques for the transport measurements and using heterodyne readout and demodulation techniques for the cQED measurements [19].

Having demonstrated the ability to probe the qubit JJ with both transport and cQED techniques, we next compare performance to a nominally identical gatemon without the FET and extra DC lead. Scanning electron

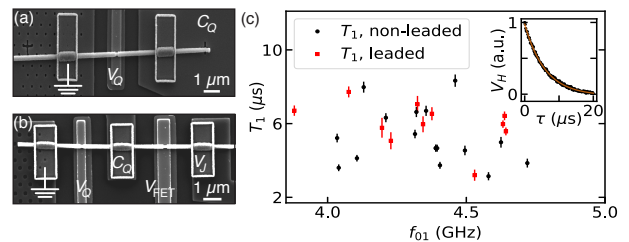


FIG. 2. (a) Scanning electron micrograph of a gatemon without transport lead. C_Q is the capacitance of the qubit island. (b) Same as (a) for gatemon with transport lead, with voltage bias V_J . (c) Qubit relaxation times T_1 of the gatemons as a function of qubit frequency, f_{01} . No overall difference between led (black circle) and non-leaded (red square) devices are observed. (Inset) Relaxation time T_1 (black points) at $f_{01} = 4.6$ GHz for the non-leaded device as a function of wait time, τ , with exponential fit (orange curve) yielding $T_1 = 6 \mu\text{s}$. Error bars are estimated from fit uncertainties.

micrographs of the two devices are shown in Figs. 2(a,b). The measured relaxation time, T_1 , is shown for a range of qubit frequencies, f_{01} , controlled by V_Q , in Fig. 2(c). The T_1 -measurements were carried out by applying a π -pulse, calibrated by a Rabi experiment at f_{01} , followed by a variable wait time τ before readout, see Fig. 2(c) inset. Values for $T_1(V_Q)$ were then extracted by fitting $V_H(\tau)$ to an exponential. We observe no systematic difference between the devices, demonstrating that the addition of a transport lead does not compromise the performance in the cQED configuration.

We next monitored dI_B/dV_B , f_{01} and T_1 as V_{FET} was varied from off (cQED regime) to on (transport regime). The dI_B/dV_B -measurement shown in Fig. 3(a) illustrates how the FET was turned conducting as V_{FET} was increased. Qubit frequency f_{01} was measured by two-tone spectroscopy, where a drive tone with varying frequency f_d was applied for $2 \mu\text{s}$, followed by a readout tone at f_R . A Lorentzian fit is used for each value of V_{FET} to extract f_{01} , see Fig. 3(b) insets. We attribute the weak dependence of f_{01} on V_{FET} to crosstalk between the two gates.

Following each spectroscopy measurement, a T_1 measurement was immediately carried out, see Fig. 3(c), yielding a nearly gate-independent value $T_1 \sim 6 \mu\text{s}$ for $V_{\text{FET}} < -2$ V. At $V_{\text{FET}} \sim -2$ V, we observe a sudden drop in T_1 , followed by a short revival at $V_{\text{FET}} \sim -1.8$ V. We associate the revival in T_1 with the corresponding drop in dI_B/dV_B observed in Fig. 3(a). For $V_{\text{FET}} > -1.5$ V, f_{01} and T_1 can no longer be resolved, consistent with the increasing dI_B/dV_B -values. We note that the dI_B/dV_B -curve in Fig. 3(a) was shifted horizontally by a small amount (0.1 V) to align features in dI_B/dV_B with corresponding features in T_1 . This was done to account for hysteresis in the gate sweep, as the cQED and transport measurements were performed sequentially with a large voltage swing on V_{FET} of ~ 3 V between the two measurements.

We develop a circuit model of qubit relaxation in the

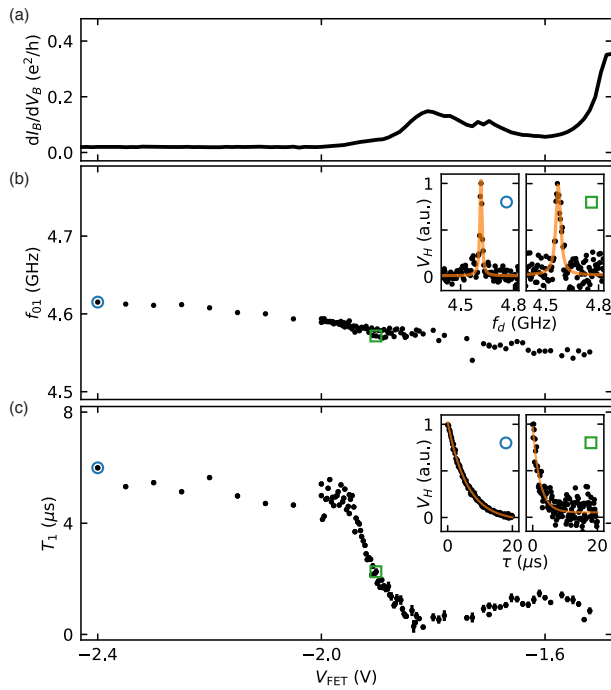


FIG. 3. (a) Differential conductance, dI_B/dV_B , as a function of FET gate voltage, V_{FET} , at high bias $V_B = 1.0\text{ mV}$, to approximate normal-state resistance. (b) Qubit frequency f_{01} as a function of V_{FET} using two-tone spectroscopy. (Insets) Lorentzian fits (orange) to data points in the main panel as indicated by the corresponding markers (blue circle, green square). From each V_H -measurement we subtract an average and normalize to the maximal value. (c) Similar to (b) relaxation times T_1 from exponential fits (Insets). Error bars are estimated from fit errors.

leaded device. Within the model, the qubit circuit is coupled through the FET to a series resistance R_F and a parallel capacitance C_F representing an on-chip filter on the lead [20]. The coupling to the environment via the (superconducting) FET junction is modelled as a gate tuneable Josephson inductance L_{FET} , giving a total envi-

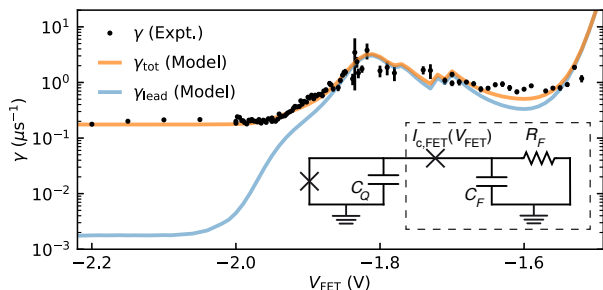


FIG. 4. Relaxation rate $\gamma = 1/T_1$ (black circles) as a function of FET voltage, V_{FET} , by inverting the experimental data from Fig. 3(c). Model relaxation rates γ_{lead} due only to the transport lead (blue) and γ_{tot} (orange) including lead and non-lead contributions (see text). The circuit model is sketched in the inset where the qubit is coupled to the environment by an effective impedance $Z_{\text{env}} = i\omega L_{\text{FET}} + (1/R_F + i\omega C_F)^{-1}$. The dashed rectangle indicates the environment circuit.

ronment impedance $Z_{\text{env}} = i\omega L_{\text{FET}} + (1/R_F + i\omega C_F)^{-1}$. This impedance can be viewed as a single dissipative element with resistance given by

$$R_{\text{env}} = 1/\text{Re}[Y] = L_{\text{FET}}^2 (R_F^2 C_F^2 \omega^4 + \omega^2) / R_F + R_F (1 - 2L_{\text{FET}} C_F \omega^2), \quad (1)$$

with admittance $Y = 1/Z_{\text{env}}$ [21]. The relaxation rate associated with the lead is given by $\gamma_{\text{lead}} = 1/R_{\text{env}} C_Q$, yielding a total decay rate $\gamma_{\text{tot}} = \gamma_{\text{nolead}} + \gamma_{\text{lead}}$, where γ_{nolead} is the decay rate associated with relaxation unrelated to the lead.

We estimate $L_{\text{FET}} = \hbar/2eI_{c,\text{FET}}$ [22], where $I_{c,\text{FET}}$ is the critical current of the FET, which we in turn relate to the normal-state resistance $R_{n,\text{FET}}$ via the relation $I_{c,\text{FET}} R_{n,\text{FET}} = \pi\Delta/2e$ [23], yielding

$$L_{\text{FET}} = \hbar R_{n,\text{FET}} / \pi\Delta. \quad (2)$$

$R_{n,\text{FET}}$ can be found from dI_B/dV_B in Fig. 3(a) by subtracting the voltage drop across the line resistance, $R_{\text{line}} = 57\text{ k}\Omega$, found by fully opening both the qubit JJ and the FET. To associate this value with $R_{n,\text{FET}}$, we assume no voltage drop across the qubit JJ, justified by $I_{c,\text{FET}} < I_c$, where I_c is the critical current of the qubit JJ. From electrostatic simulations we estimate $C_Q = 38\text{ fF}$ [24]. We take $\omega = 2\pi\bar{f}_{01}$, where $\bar{f}_{01} = 4.6\text{ GHz}$ is the average f_{01} in Fig. 3(b), and $\Delta = 190\text{ }\mu\text{eV}$ from Fig. 1(d). Combining Eqs. 1 and 2 with the measured $1/T_1$ -data, yields the γ_{lead} -result in Fig. 4 using $R_F = R_{\text{line}}$ and $C_F = 0.1\text{ pF}$ as the best fit parameter. We note that electrostatic simulations give $C_F \sim 0.5\text{ pF}$, in reasonable agreement with the best fit value. We define $\gamma_{\text{nolead}} = 1/T_1^{\text{mean}}$, where $T_1^{\text{mean}} = 5.8\text{ }\mu\text{s}$ is the mean value of the T_1 at $V_{\text{FET}} < -2\text{ V}$. Using this estimate for γ_{nolead} , we calculate the total relaxation time based on the transport data (orange line in Fig. 4) showing excellent agreement with the measured values. The T_1 -limit based on the contribution of the lead saturates at $T_{1,\text{lead}} \sim 1\text{ ms}$, indicating that leaded gatemon devices can accommodate large improvements in gatemon relaxation times.

Combining transport and cQED measurements allows for the correlation between critical current $I_c(V_Q)$ and $f_{01}(V_Q)$ to be observed directly. The critical current I_c is extracted from dI_B/dV_B and I_B while sweeping V_B and V_Q . We extract the voltage drop and differential resistance across the qubit junction, V_J and dV_J/dV_B , by inverting dI_B/dV_B and subtracting R_{line} . In doing this we assume that there is no voltage drop across the FET junction, since $I_c < I_{c,\text{FET}}$. The qubit resonance f_{01} is measured over the same V_Q range using two-tone spectroscopy, see Fig. 5(b). We note that the two-photon transition to the next harmonic is also observed for some V_Q -values, visible at a slightly lower frequency than f_{01} , given by the anharmonicity.

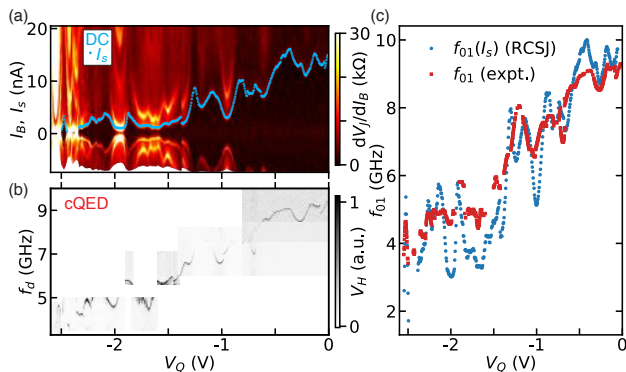


FIG. 5. (a) Differential resistance of the qubit JJ, dV_J/dI_B , as a function of current bias I_B and qubit gate voltage, V_Q . Switching current, I_s , (blue points) from the edge of the zero-resistance state for increasing sweep at $V_{\text{FET}} = +4$ V to turn the FET conducting. (b) Qubit frequency, f_{01} , from two-tone spectroscopy as a function of V_Q , acquired at $V_{\text{FET}} = -3$ V to deplete the FET. The area of missing data at 5.0–5.6 GHz is due to f_{01} crossing the resonator frequency, f_R . (c) Correlation between transport and cQED data. f_{01} from (b) (red) extracted as in Fig. 3(b) (inset). f_{01} from I_c (blue) extracted by applying an RCSJ model to the data in (a) (see text).

The relation between the two measurements is shown in Fig. 5(c). In order to estimate $I_c(V_Q)$ we first extract the switching current $I_s(V_Q)$ from the data, taken as the I_B -value at which dV_J/dI_B is maximal, while sweeping I_B from negative to positive values [blue dots in Fig. 5(a)]. Bright features at high bias ($I_B > I_s$) are likely associated with multiple Andreev reflection (MAR) [25]. To extract I_c from the measured I_s , we model the qubit JJ as an underdamped RCSJ junction with a sinusoidal current-phase relation $I = I_c \sin \phi$. Furthermore, we note the small difference between the return current I_r (same definition as I_s at negative I_B) is slightly smaller than I_s [26]. In this case, I_s corresponds to the current of equal stability between the resistive and non-resistive state [27]. Under this condition, and for large quality factors, $Q \gg 1$, the ratio I_s/I_c depends on quality factor $Q = R\sqrt{2eI_cC_Q/\hbar}$ as

$$I_s/I_c = (2 + 4/\pi)Q^{-1} + (2 + \pi)Q^{-2}, \quad (3)$$

where $R = (1/R_J + 1/R_{\text{line}})^{-1}$ and R_J is the shunt resistance [27]. For simplicity, we take R_J to be equal to the normal state resistance of the junction, R_N . We then apply the Ambegaokar-Baratoff relation $I_cR_J = \pi\Delta/2e$ [23], which allows us to extract I_c by inverting Eq. 3 numerically [28]. The extracted values of I_c , in turn, yield values for Q in the range 10-20, consistent with our initial assumptions. For these values of Q , the RCSJ model takes the electron temperature to be > 50 mK to account for the weak asymmetry in I_s and I_r [26]. Finally, we relate I_c to f_{01} by using the numerical solution of the standard transmon Hamiltonian,

$H = 4E_C(n - n_g)^2 - E_J \cos(\phi)$ [29], with $E_J = \hbar I_c/2e$ and $E_C/\hbar = e^2/2\hbar C_Q = 512$ MHz, at the charge degeneracy point with offset charge $n_g = 0.5$.

A comparison of the measured and estimated f_{01} is shown in Fig. 5(c). The model (RCSJ) curve is shifted horizontally by 0.05 V to align the features at ~ -2.5 V and can be attributed to small gate hysteresis. A clear correlation is observed between the two measurement techniques, especially evident from the matching of local minima and maxima of both spectra and the overall agreement of the absolute values. We attribute the residual quantitative discrepancy to the simplifying assumptions used to determine the shunt resistance of the RCSJ model, which likely do not capture the possible gate dependence of the subgap DOS of the qubit JJ. In addition, the assumption of sinusoidal CPR will break down as the qubit JJ is opened due to increasing mode transmission in the semiconductor junction, leading to small overshoots of the model as perhaps seen around $V_Q \sim 0$ V.

In summary, we have demonstrated the compatibility of DC transport and cQED measurement techniques in gatemon qubits. This method may extend to other material platforms such as two-dimensional electron gases [15] or graphene [16, 30]. Furthermore, we achieve a controllable relaxation rate potentially relevant for a range of qubit applications such as tunable coupling schemes [31, 32], and controlled qubit relaxation and reset protocols [33, 34]. In addition, we have demonstrated clear correlation between DC transport and cQED measurements motivating future extensions, such as studying CPRs [8] or probing channel transmissions by studying multiple Andreev reflections [12] combined with cQED experiments [10, 13, 14]. Combining well-established transport techniques in quantum dot physics with qubit geometries may also be an interesting research direction [35]. Potentially this geometry is also a promising platform to coherently probe Majorana zero modes in cQED measurements [36], as transport signatures have been demonstrated, both in half-shell nanowires [37] and full-shell wires [38, 39].

This work was supported by Microsoft and the Danish National Research Foundation. We acknowledge Robert McNeil, Marina Hesselberg, Agnieszka Telecka, Sachin Yadav, Karolis Parfeniukas, Karthik Jambunathan and Shivendra Upadhyay for the device fabrication. We thank Lucas Casparis and Roman Lutchyn for useful discussions, as well as Ruben Grigoryan for input on the electronic setup. BvH would like to thank the Center of Quantum Devices, Niels Bohr Institute for the hospitality during the time in which this study was carried out.

-
- [1] M. H. Devoret and R. J. Schoelkopf, *Science* **339**, 1169 (2013).
- [2] H. Paik, D. I. Schuster, L. S. Bishop, G. Kirchmair, G. Catelani, A. P. Sears, B. R. Johnson, M. J. Reagor, L. Frunzio, L. I. Glazman, S. M. Girvin, M. H. Devoret, and R. J. Schoelkopf, *Phys. Rev. Lett.* **107**, 240501 (2011).
- [3] L. Bretheau, Ç. Ö. Girit, H. Pothier, D. Esteve, and C. Urbina, *Nature* **499**, 312 (2013).
- [4] Y.-J. Doh, J. A. van Dam, A. L. Roest, E. P. A. M. Bakkers, L. P. Kouwenhoven, and S. De Franceschi, *Science* **309**, 272 (2005).
- [5] T. W. Larsen, K. D. Petersson, F. Kuemmeth, T. S. Jespersen, P. Krogstrup, J. Nygård, and C. M. Marcus, *Phys. Rev. Lett.* **115**, 127001 (2015).
- [6] G. de Lange, B. van Heck, A. Bruno, D. J. van Woerkom, A. Geresdi, S. R. Plissard, E. P. A. M. Bakkers, A. R. Akhmerov, and L. DiCarlo, *Phys. Rev. Lett.* **115**, 127002 (2015).
- [7] A. A. Golubov, M. Y. Kupriyanov, and E. Il'ichev, *Rev. Mod. Phys.* **76**, 411 (2004).
- [8] E. M. Spanton, M. T. Deng, S. Vaitiekėnas, P. Krogstrup, J. Nygård, C. M. Marcus, and K. A. Moler, *Nat. Phys.* **13**, 1177 (2017).
- [9] M. Tinkham, *Introduction to superconductivity* (Courier Corporation, 2004).
- [10] L. Tosi, C. Metzger, M. F. Goffman, C. Urbina, H. Pothier, S. Park, A. L. Yeyati, J. Nygård, and P. Krogstrup, *Phys. Rev. X* **9**, 011010 (2019).
- [11] K. Zuo, V. Mourik, D. B. Szombati, B. Nijholt, D. J. van Woerkom, A. Geresdi, J. Chen, V. P. Ostroukh, A. R. Akhmerov, S. R. Plissard, D. Car, E. P. A. M. Bakkers, D. I. Pikulin, L. P. Kouwenhoven, and S. M. Frolov, *Phys. Rev. Lett.* **119**, 187704 (2017).
- [12] M. F. Goffman, C. Urbina, H. Pothier, J. Nygård, C. M. Marcus, and P. Krogstrup, *New Journal of Physics* **19**, 092002 (2017).
- [13] A. Kringhøj, L. Casparis, M. Hell, T. W. Larsen, F. Kuemmeth, M. Leijnse, K. Flensberg, P. Krogstrup, J. Nygård, K. D. Petersson, and C. M. Marcus, *Phys. Rev. B* **97**, 060508 (2018).
- [14] M. Hays, G. de Lange, K. Serniak, D. J. van Woerkom, D. Bouman, P. Krogstrup, J. Nygård, A. Geresdi, and M. H. Devoret, *Phys. Rev. Lett.* **121**, 047001 (2018).
- [15] L. Casparis, M. R. Connolly, M. Kjaergaard, N. J. Pearson, A. Kringhøj, T. W. Larsen, F. Kuemmeth, T. Wang, C. Thomas, S. Gronin, G. C. Gardner, M. J. Manfra, C. M. Marcus, and K. D. Petersson, *Nat. Nanotechnol.* **13**, 915 (2018).
- [16] J. I.-J. Wang, D. Rodan-Legrain, L. Bretheau, D. L. Campbell, B. Kannan, D. Kim, M. Kjaergaard, P. Krantz, G. O. Samach, *et al.*, *Nat. Nanotechnol.* **14**, 120 (2019).
- [17] J. J. Riquelme, L. de la Vega, A. L. Yeyati, N. Agrat, A. Martin-Rodero, and G. Rubio-Bollinger, *Europhysics Letters (EPL)* **70**, 663 (2005).
- [18] P. Krogstrup, N. L. B. Ziino, W. Chang, S. M. Albrecht, M. H. Madsen, E. Johnson, J. Nygård, C. M. Marcus, and T. S. Jespersen, *Nat. Mater.* **14**, 400 (2015).
- [19] See Supplementary Material for additional details on the experimental setup.
- [20] X. Mi, J. Cady, D. Zajac, J. Stehlik, L. Edge, and J. R. Petta, *Applied Physics Letters* **110**, 043502 (2017).
- [21] A. A. Houck, J. A. Schreier, B. R. Johnson, J. M. Chow, J. Koch, J. M. Gambetta, D. I. Schuster, L. Frunzio, M. H. Devoret, S. M. Girvin, and R. J. Schoelkopf, *Phys. Rev. Lett.* **101**, 080502 (2008).
- [22] S. M. Girvin, in *Quantum Machines: Measurement and Control of Engineered Quantum Systems*, Lecture Notes of the Les Houches Summer School: Volume 96, July 2011 (Oxford University Press, 2014).
- [23] V. Ambegaokar and A. Baratoff, *Phys. Rev. Lett.* **11**, 104 (1963).
- [24] COMSOL, Inc. [www.comsol.com].
- [25] T. Klapwijk, G. Blonder, and M. Tinkham, *Physica B+C* **109**, 1657 (1982).
- [26] See Supplementary Material for additional details on the critical current analysis.
- [27] R. L. Kautz and J. M. Martinis, *Phys. Rev. B* **42**, 9903 (1990).
- [28] Numerical code and data accompanying the analysis of Fig. 5(c) is found at: https://github.com/anderskringhoej/dc_qubit.
- [29] J. Koch, T. M. Yu, J. M. Gambetta, A. A. Houck, D. I. Schuster, J. Majer, A. Blais, M. H. Devoret, S. M. Girvin, and R. J. Schoelkopf, *Phys. Rev. A* **76**, 042319 (2007).
- [30] J. Kroll, W. Uilhoorn, K. van der Enden, D. de Jong, K. Watanabe, T. Taniguchi, S. Goswami, M. Cassidy, and L. Kouwenhoven, *Nat. Commun.* **9**, 4615 (2018).
- [31] Y. Chen, C. Neill, P. Roushan, N. Leung, M. Fang, R. Barends, J. Kelly, B. Campbell, Z. Chen, B. Chiaro, A. Dunsworth, E. Jeffrey, A. Megrant, J. Y. Mutus, P. J. J. O'Malley, C. M. Quintana, D. Sank, A. Vainsencher, J. Wenner, T. C. White, M. R. Geller, A. N. Cleland, and J. M. Martinis, *Phys. Rev. Lett.* **113**, 220502 (2014).
- [32] L. Casparis, N. J. Pearson, A. Kringhøj, T. W. Larsen, F. Kuemmeth, J. Nygård, P. Krogstrup, K. D. Petersson, and C. M. Marcus, *Phys. Rev. B* **99**, 085434 (2019).
- [33] P. J. Jones, J. A. M. Huhtamäki, J. Salmilehto, K. Y. Tan, and M. Möttönen, *Scientific Reports* **3**, 1987 EP (2013).
- [34] R. Ma, B. Saxberg, C. Owens, N. Leung, Y. Lu, J. Simon, and D. I. Schuster, *Nature* **566**, 51 (2019).
- [35] S. De Franceschi, L. Kouwenhoven, C. Schönenberger, and W. Wernsdorfer, *Nat. Nanotechnol.* **5**, 703 (2010).
- [36] E. Ginossar and E. Grosfeld, *Nat. Commun.* **5**, 4772 EP (2014).
- [37] V. Mourik, K. Zuo, S. M. Frolov, S. R. Plissard, E. P. A. M. Bakkers, and L. P. Kouwenhoven, *Science* **336**, 1003 (2012).
- [38] R. M. Lutchyn, G. W. Winkler, B. Van Heck, T. Karzig, K. Flensberg, L. I. Glazman, and C. Nayak, *arXiv preprint arXiv:1809.05512* (2018).
- [39] S. Vaitiekėnas, M.-T. Deng, P. Krogstrup, and C. M. Marcus, *arXiv preprint arXiv:1809.05513* (2018).

SUPPLEMENTARY MATERIAL

Experimental setup

The measurements presented in the paper are conducted in a cryogen-free dilution refrigerator with a base temperature of ~ 10 mK. A detailed schematic of the electronic setup is shown in Fig. S1. The sample is mounted to a Cu circuit board located in an indium sealed CuBe box mounted inside another Cu box, which is thermally attached to the mixing chamber plate. DC lines (blue lines in Fig. S1) connect to the sample through a loom heavily filtered at frequencies above 80 MHz via both the QDevil and the LFCN-80 low pass filters. For transport measurements we measure a small AC current using the SR860 lock-in amplifier while also measuring the DC current to ground with the Keysight multimeter. Both current signals are amplified and converted to a voltage by the Basel SP983 I-to-V converter.

Two microwave coaxial drive lines connect to the sample (red lines in Fig. S1). The combined input signal is generated by two RF sources and is heavily attenuated and filtered above 10 GHz with a K&L low pass filter. These two signals are used for qubit drive and readout drive, respectively. The output signal is again filtered and amplified at the 4 K stage with a cryogenic low noise amplifier with a bandwidth of 4–8 GHz with further amplification at room temperature using the Miteq amplifier. The output signal is down converted to an intermediate frequency by mixing with a local oscillator and filtering of the high frequency component. After another amplification stage using the SR445A amplifier, the intermediate frequency signal is digitized and digitally down converted in order to extract the in-phase and quadrature components of the readout signal.

The SR FS725 10 MHz clock reference is connected to the Alazar card, signal generators and the AWG for synchronisation of the microwave signals.

RCSJ modelling details and data

To supplement the data and the analysis presented in Fig. 5, we measured dV_J/dI_B as a function of I_B and V_Q for a I_B -range where we were able to extract both I_s and I_r for the entire V_Q -range, see Fig. S2(a). This dataset shows quantitatively almost the same features as the dataset in the main text. However, due to a larger amount of drift, possibly due to longer acquisition time, we use the dataset in Fig. 5(a) to perform the modelling in the main text. From the measurement shown in Fig. S2(a) we are able to extract both I_s and I_r , see Fig. S2(b). Here we observe a weak asymmetry between I_r and I_s for the full V_Q -range, which justifies the use of the RCSJ model applied in the analysis of Fig. 5(c).

In addition, we compute the extracted critical current I_c and $E_J = \hbar I_c/2e$ used in our RCSJ analysis, as shown in Fig. S2(c). Based on these E_J -values we estimate the electron temperature T to be > 50 mK, such that the $k_B T/E_J$ -ratios account for the weak asymmetry between I_r and I_s [27]. To further justify the application of the $Q \gg 1$ limit, we numerically extract the Q -values, as shown in Fig. S2(d).

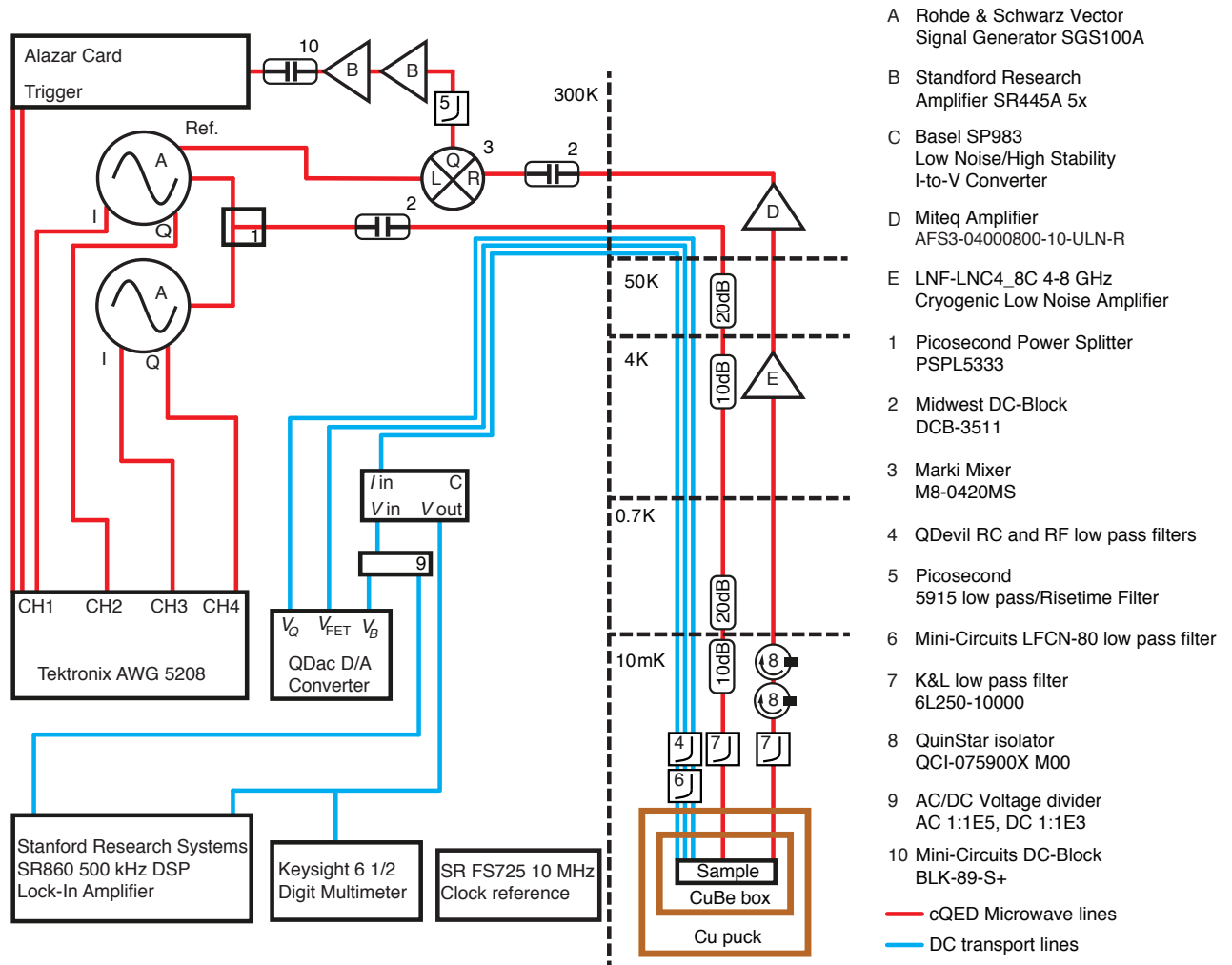


FIG. S1. Schematic of the setup. Blue lines refer to lines used for the DC transport and red lines are the microwave drive lines used for qubit manipulation and readout. The signal generators, AWG, and Alazar card are all connected to the SR FS725 10 MHz clock reference for synchronisation.

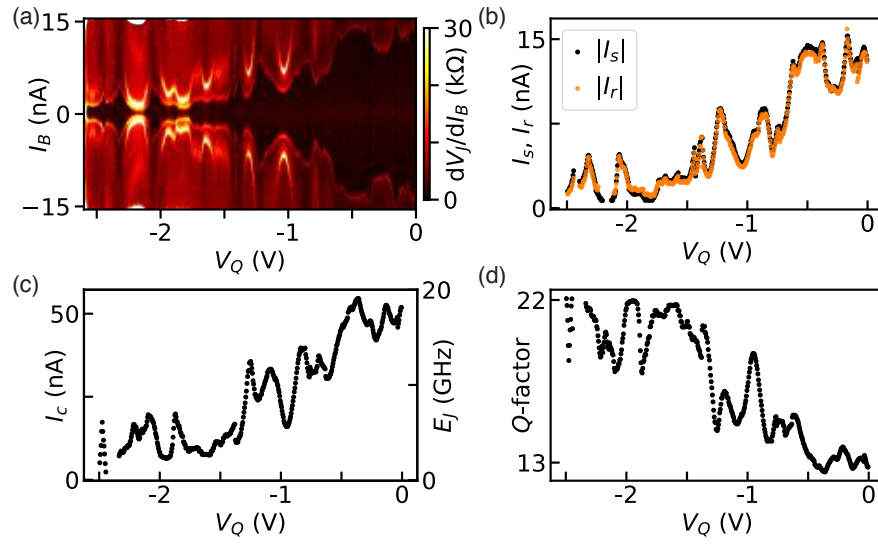


FIG. S2. (a) DC transport measurement of dV_J/dI_B as a function of I_B and V_Q , acquired in the same way as the data presented in Fig. 5(a). In this measurement, both the transition to a non-resistive state at negative I_B -values and the transition to the resistive state at positive I_B -values are observed. (b) Absolute values of the extracted return current I_r and switching current as a function of V_Q , illustrating the weak asymmetry in their values. (c) Extracted critical current I_c (left y -axis, converted to $E_J = \hbar I_c/2e$ on the right y -axis). (d) Extracted quality factor Q from the numerical solutions to Eq. 3.